metals

MDPI

Article

Formability Assessment Based on Q-Value for Optimizing the Deep Drawing Process of Automotive Parts Made from Aluminum Alloys Sheet

Jidapa Leelaseat, Aekkapon Sunanta and Surasak Suranuntchai *

Department of Tool and Materials Engineering, King Mongkut's University of Technology Thonburi, 126 Pracha Uthit Rd., Bang Mod, Thung Khru, Bangkok 10140, Thailand; jidapa.leel@kmutt.ac.th (J.L.); aekkapon.sunan@mail.kmutt.ac.th (A.S.)

* Correspondence: surasak.sur@kmutt.ac.th

Abstract: This paper presents a novel Q-value-based formability assessment for optimizing deep drawing processes. The Q-value, derived from thinning limit diagrams (TLDs), uses offset thinning and wrinkling limit curves to define severity levels. It is calculated by summing the product of Pascal's triangle weighting factors and normalized element counts within each severity level. The effectiveness of this Q-value assessment was demonstrated using experimentally validated finite element analysis (FEA) to optimize blank size, tool geometry, and drawbead design (male bead height and contra-bead radius) for a deep-drawn AA5754-O automotive fuel tank. Validation of FEA results with experimental thickness measurements showed that the Barlat and Lian 1989 yield criterion provided higher accuracy than Hill's 1948 model. An optimal condition, determined using the Q-value, consists of a 430 mm × 525 mm blank formed by a redesigned tool cooperated with optimized semi-circular drawbead geometries, achieving experimental significant formability improvements by minimizing wrinkling and thinning. During optimization, this study revealed a significant interaction between blank width and length, which influenced formability. Side-wall wrinkles were attributed to insufficient tool support for the blank during forming and were relieved through tool redesign. Furthermore, increasing the male drawbead height effectively reduced wrinkling but led to increased thinning, whereas increasing the contra-bead radius had the opposite effect.

Keywords: formability; deep drawing process; optimization; finite element simulation; automotive part; aluminum alloys sheet

check for updates

Academic Editors: Gang Fang and Chaoyang Sun

Received: 28 November 2024
Revised: 8 January 2025
Accepted: 10 January 2025
Published: 14 January 2025

Citation: Leelaseat, J.; Sunanta, A.; Suranuntchai, S. Formability Assessment Based on Q-Value for Optimizing the Deep Drawing Process of Automotive Parts Made from Aluminum Alloys Sheet. *Metals* **2025**, *15*, 68. https://doi.org/10.3390/met15010068

Copyright: © 2025 by the authors. Licensee MDPI, Basel, Switzerland. This article is an open access article distributed under the terms and conditions of the Creative Commons Attribution (CC BY) license (https://creativecommons.org/licenses/by/4.0/).

1. Introduction

Deep drawing, a fundamental sheet metal forming process that is crucial to the automotive industry, enables the shaping of complex hollow parts [1,2] like cylinder head covers, oil pans, support plates, and fuel tanks. Sometimes, due to the geometrical complexity and large deformation involved during the process, undesired defects like wrinkles, severe thinning, and tearing possibly occur in the deep drawn parts [3–5].

Drawability refers to a material's ability to undergo deformation in the deep drawing process without failure. To assess drawability, there are different methods depending on the scale and complexity of the forming process. At the laboratory scale, drawability is often indicated by a quantifier known as the limiting drawing ratio (LDR). By a cylindrical cup drawing test, the LDR is defined as the ratio of the maximum drawable blank diameter that is determined by testing a series of incrementally larger blanks to the punch diameter

where cracking first appears [6]. On the other hand, in automotive manufacturing, parts are often complex, like non-rotational symmetric parts that non-uniformly deform around the axis and are usually formed by a multi-forming process. Therefore, LDR may not be an extensive drawability indicator.

According to the advancement of finite element analysis (FEA), characteristics of the forming material like post-forming shapes, terms of load and displacement values, thickness distribution, and potential failure zones can be predicted by the finite element method with properly selected material models for numerical solving [7–11]. FEA facilitates significant resource savings in both the design and optimization stages of manufacturing processes, especially for industrial-scale parts. These savings include reduced machine power and labor costs, extended tool life, and minimized material waste. For this reason, the drawability assessments on the issue of crack and wrinkle occurrence in industrial parts are used in FEA applications. Conventionally, the strain-based forming limit diagram (ε-FLD) is widely used to analyze strain paths in relation to the forming limit curve (FLC) and wrinkling limit curve. By comparing the strain path to these curves, it is possible to determine whether the path is safe or at risk of necking [12–16] or wrinkling [17–19], respectively. Meanwhile, a common quality requirement for load-bearing components is a limit on the permissible percentage of thinning, often specified by customers to address concerns about excessive thinning [20,21]. In practice, if the maximum thinning on a part exceeds this limit, the part is rejected.

In the process of formability improvement, the influenced parameters such as tool geometry and process operating parameters are typically adjusted. Forming limit diagrams (FLDs) before and after these adjustments are compared to assess the improvements. Observing the results of the improvements can be challenging, especially when the differences in the FLDs are not obvious and result in the same outcome (safe/fail). Moreover, comparing the maximum thinning percentage on the part to the permissible limit focuses only on the maximum value and neglects an analysis of how thinning trends developed in the rest of the part during the formability improvement process.

The aforementioned limitations have led to the proposal of the thinning limit diagram (TLD), which integrates the forming limit with thinning across the entire part. The TLD allows for the classification of safe and failure zones based on the observed behavior of thinning and thickening (negative thinning values). With perspective that the thickness change from the nominal thickness of the prepared blank is the result from the deformation of the blank under the assumption of volume constancy during plastic deformation, this implies that the closeness of the element's thinning value to the thinning limit curve (TLC), and to the wrinkling limit curve in the TLD space, correlates with its risk of necking and wrinkling, respectively. Hence, to quantify formability beyond the simple safe/fail classification of the TLD and conventional FLD, a novel quantifier termed the Q-value was developed. The Q-value is calculated by summing the weighted values representing the severity of thinning across the part. To achieve this, both the thinning limit curve and wrinkling limit curve are offset into a number of curves (representing different levels of severity), and the corresponding weight factors for each level are multiplied by the ratio of elements within each level to the total number of elements. Assigning these weighted severity levels allows for a fair comparison between simulations (when simulation settings of the simulations are consistent).

In this study, we propose a novel formability assessment method based on the Q-value. The proposed approach offers a practical and quantitative evaluation of formability by capturing the severity of thinning across the entire part. By enabling detailed comparisons between parameter settings in forming simulations, the Q-value provides insights into whether formability improves or worsens. Unlike traditional FLD-based assessments, this

method delivers a more comprehensive and systematic analysis, making it highly effective for optimizing process parameters.

To validate the effectiveness of this novel method, the method was applied to investigate the influence of key parameters on the formability of parts in the deep drawing process. Factors such as blank holder force [22–25], forming temperature [26–28], punch/die profile radii [29,30], initial blank thickness [31,32], and relative die clearance [33,34] have been extensively studied. However, the effect of blank size has received less attention. Previous studies have shown that blank size significantly affects thickness distribution and formability in circular [35] and square blanks [36]. For rectangular blanks, Leelaseat et al. [37] demonstrated that adjusting blank length (while keeping width constant) can reduce defects like side-wall wrinkling and thinning within a specific range, although excessive length may induce wrinkling. Building on this, the present study investigates the effect of varying both the length and width of rectangular blanks. And if the side-wall wrinkling persists after optimizing the blank size, drawbead addition, a practical technique, will be incorporated. Drawbeads provide localized control of material flow [38–40] but can negatively impact formability by inducing plane strain deformation (which is known to be a low forming limit state [41]). By optimizing the rectangular blank size, this study hypothesizes that the reliance on drawbeads for controlling material flow can be reduced, potentially minimizing their negative impact on formability.

The formability assessment is applied to investigate the effects of blank size (length and width) and drawbead geometries, aiming to identify optimal values for the final part's formability. Analysis of simulated thickness distributions, TLDs, and stress distributions, corroborated by experimental forming results, will demonstrate the utility of the novel assessment method in evaluating and optimizing formability, as well as its potential applicability to other relevant parameters in future studies.

2. Quantitative Evaluation of Formability Using Thinning Limit Diagrams and Pascal's Triangle Weighting Factors

2.1. Thinning Limit Diagram

The thinning limit diagram (TLD) is a diagram that plots in space where the engineering function of minor strain (e_2) was represented on the x-axis and the percentage of thinning on the y-axis. The diagram consists of two primary components, first is the strain path, which is the data of element deformation in coordinates space, and the second is limit curves consist of the thinning limit curve (TLC) and wrinkling limit curve (WLC).

Thinning is a value of the change in thickness (Δt) that relates to the initial thickness (t_0) of the blank as Equation (1) and is usually used in percentage value as Equation (2).

$$\text{Thinning} = e_t = \Delta t / t_0 \tag{1}$$

$$\%\ \text{Thinning} = 100\% \times \text{Thinning} \tag{2}$$

We use the principle of volume constancy during plastic deformation, as described in Equation (3), which is in terms of principal strains (ε_1, ε_2 in the plane of the blank, and ε_3, which corresponds to ε_t thickness strain), as in Equation (4).

$$\varepsilon_{volume} = \ln (V_{int}/V_0) = \ln (1) = 0 \tag{3}$$

$$\varepsilon_1 + \varepsilon_2 + \varepsilon_3 = 0 \tag{4}$$

where V_{int} represents the instantaneous volume and V_0 represents the initial volume.

This leads to the %Thinning value derived from major and minor strain by Equation (5).

$$\%\text{Thinning} = -100\% \times \left(e^{-(\varepsilon_1+\varepsilon_2)} - 1\right) \tag{5}$$

The TLC in this study is derived from the strain-based forming limit curve (ε-FLC). While WLC within the TLD is derived from the WLC within the principal strain space. The WLC within the principal strain space is normally characterized by exhibiting positive thickness strain (associated to pure shear state). This is supported by studies by Panich and Uthaisangsuk [42] about the initiate of wrinkling on AA5052-O and AA5052-H32 by modified Yoshida buckling tests, and they found that WLCs are linear in principal the strain space between the uniaxial tension state, whose strain ratio ($\varepsilon_1/\varepsilon_2$) is −0.5, and the pure shear state (strain ratio −1 where $\varepsilon_1 = -\varepsilon_2$ and $\varepsilon_3 = 0$). Also, in 304 stainless steel at varied initial thicknesses of prepared blanks by Du et al. [18], the linear WLC also located the pure shear state.

2.2. Thinning Limit Diagram with Severity Levels via Offset Limit Curves

The limit curves comprise a thinning limit curve, representing the upper boundary of thinning before necking, and a wrinkling limit curve, representing the lower boundary of thinning (this is because wrinkling occurs due to material buckling under compressive stresses through the thickness, resulting in thickening [43], which is represented by negative thinning values).

Marginal zones of both limit curves are determined based on the determiner's acceptable thinning variations for part functionality for how many percentages offset (in this study called severity percentage: *SP*%) from the TLC and WLC curves to the separate necking zone, safe zone, and wrinkling zones. For finer analysis, the marginal zones are further divided into levels, each interval's width equal to *i*% of curves. We obtained the total number of intervals calculated by Equation (6) that includes the number of intervals in marginal zones, safe zone, excessive thinning zone (over the TLC), and excessive thickening zone (below the WLC).

This results in varying widths for the marginal zones and levels for the TLC and WLC, as depicted in Figure 1. The TLC and WLC offsets recognize the different underlying mechanisms governing necking and wrinkling.

$$\text{Number of intervals} = ((SP\%/i\%) \times 2) + 3 \quad (6)$$

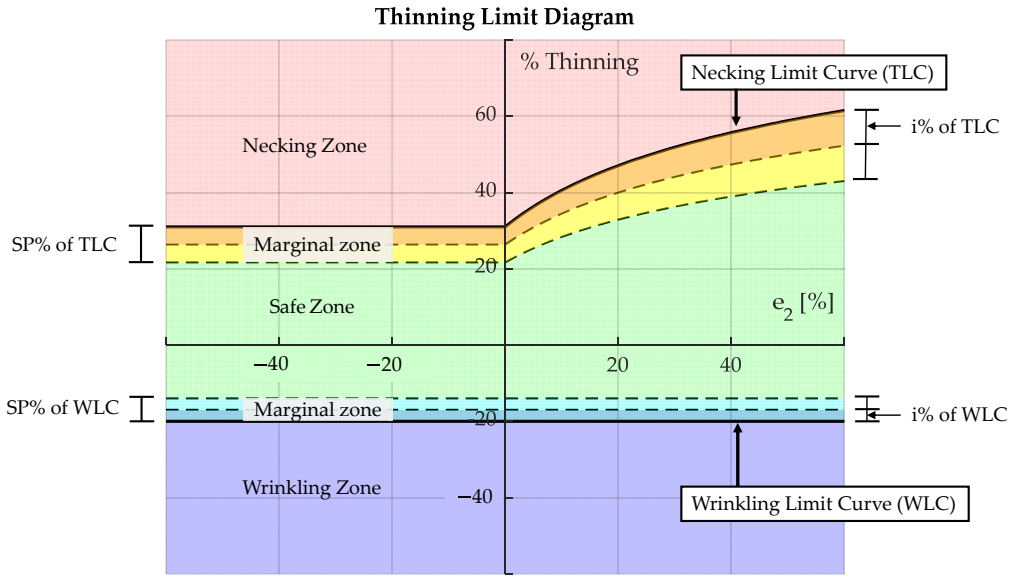


Figure 1. Schematic diagram of thinning limit diagram with severity levels via offset limit curves (*SP*%: severity percentage, *i*%: percentage of interval's width).

2.3. Formability Quantifier: Q-Value and Its Calculation

The proximity of an element's thinning value to the forming limit curves (TLC and WLC) within the TLD indicates the severity of necking and wrinkling risks. This concept led to the development of the thinning limit diagram with severity levels, created by offsetting the limit curves. These offset curves define multiple intervals, including a safe zone interval, a necking trend zone, a wrinkling trend zone, and a number of intervals within the marginal zones, as previously explained in Section 2.2 and depicted in Figure 1.

To enable quantitative comparisons of formability improvements beyond the limitations of traditional safe/fail assessments based on FLDs, a single scalar value, the Q-value, is introduced. The Q-value represents the overall formability of the formed part by aggregating the volumetric distribution of elements across the severity levels. Furthermore, it implicitly accounts for proximity to both the TLC and WLC, making it sensitive to both necking and wrinkling tendencies. Consequently, the weighted sum method is proposed for calculating the Q-value.

The Q-value is derived by summing the products of weighting factors (representing the severity of each interval) and the proportion of elements within each interval relative to the total number of elements, as expressed in Equation (7).

$$\text{Q-value} = \sum_{k=1}^{\text{Number of interval}} W_k \times \left(\frac{\text{number of elements in interval } k^{th}}{\text{total number of elements}} \right) \quad (7)$$

where k is regulated to start 1 from the necking zone interval (above TLC) and end where the interval of wrinkling zone is.

To calculate the Q-value effectively, it is essential to assign appropriate weighting factors (W_k) to each interval, reflecting their relative severity. Pascal's triangle offers a practical and mathematically robust solution for deriving these weighting factors, ensuring both flexibility and significant differentiation across intervals, as detailed in the following.

Weighting Factors: Pascal's Triangle Number

The weighting factor (W_k) for each interval is determined to support flexibility in the number of intervals, allowing users to customize severity percentages *SP*% and interval percentages *i*%, as shown in Equation (6), while also ensuring significant differences between weighting factors.

Pascal's triangle, named after the French mathematician, Blaise Pascal, possesses unique properties that have been utilized in various applications across different cultures throughout history [44]. The coefficients can be calculated by using a combination formula:

$$W_k = \binom{n}{k-1} = \binom{n-1}{k-1} + \binom{n-1}{k-2} = \frac{n!}{(n-(k-1))! \times (k-1)!} \quad (8)$$

where n and k represent the nth row and kth column of Pascal's triangle.

In this equation, n is related to the number of intervals as n = number of intervals − 1, and k is the integer range [1, numbers of intervals]. This formulation offers flexibility, as the values are calculated solely based on the number of intervals derived from Equation (6). Thus, it is adaptable to user-defined severity percentages and interval percentages.

The use of Pascal's triangle is advantageous due to its straightforward calculation (Equation (8)) and its inherent capability to generate a distribution that approximates a normal distribution. This characteristic results in significant differences between the weighting factors, as demonstrated for the tenth row of the triangle in Figure 2. Consequently, Pascal's triangle coefficients are employed for assigning severity weights.

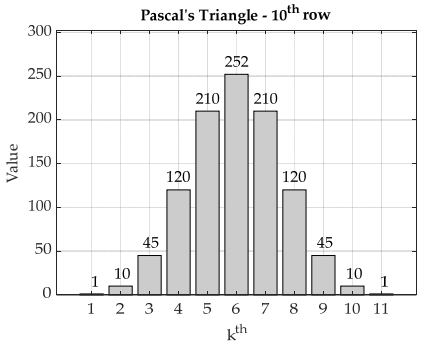


Figure 2. Tenth row of Pascal's triangle.

According to the fact that weighting factors derived from Pascal's triangle follow a normal distribution shape, intervals near the center (safe zone) are assigned higher weighting values while intervals farther from the center (toward necking and wrinkling zones) are assigned smaller weights. In Equation (7), k is defined to start at 1 from the necking zone interval (above TLC) and end at the interval of the wrinkling zone. This alignment places the safe zone interval at the center, receiving the highest weighting value, while intervals farther away are weighted less. Therefore, when comparing Q-values for formability assessment, a higher Q-value signifies better formability. And the overview of the detailed procedure for finding the Q-value is described below in Figure 3.

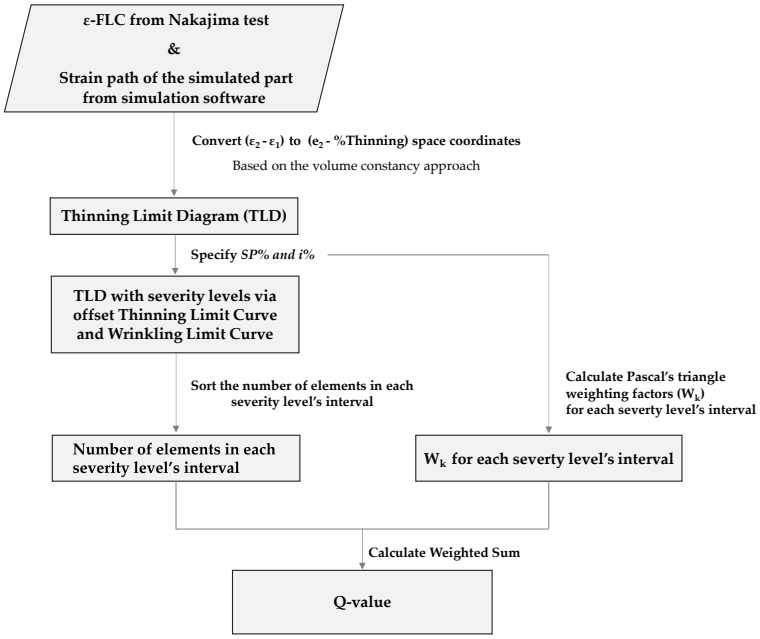


Figure 3. Procedure for finding Q-value.

3. Methodology

3.1. Material and Mechanical Properties

A commercial rolled aluminum alloy sheet (AA5754-O) with a nominal thickness of 1.5 mm was used in this study. The material has a Poisson's ratio of 0.33 and a density of 2.7×10^{-6} kg/mm^3. The major alloying element is magnesium, with a concentration approximate to 2.8 weight percent. More detailed composition information and results from uniaxial tensile tests, performed according to ASTM E8 [45], are available in a previous study [37]. The key mechanical properties are summarized in Table 1.

Table 1. The material's mechanical properties.

Properties [Unit]	Values
Ultimate Tensile Strength [MPa]	207.64
Elastic Modulus [GPa]	70.24
Yield Strength (σ_0) [MPa]	100.17
Total Elongation [%]	21.87
r_0	0.57
r_{45}	0.80
r_{90}	0.68

The constitutive relationship between stress and plastic strain, obtained from specimens oriented longitudinally to the rolling direction, was plotted and fitted using Swift's hardening law [46]:

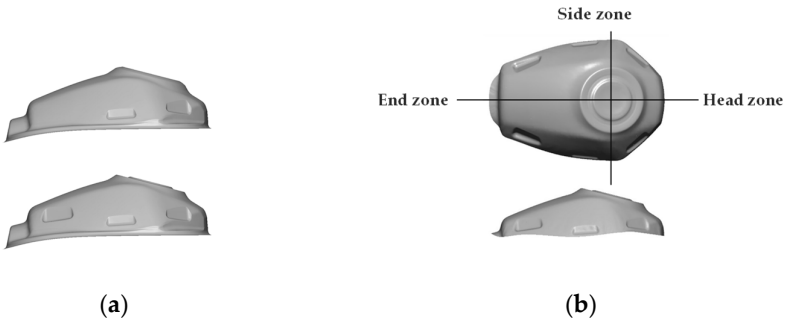
$$\overline{\sigma}(\overline{\varepsilon}) = 396.5 \times (\overline{\varepsilon} + 0.00595)^{0.26} \text{in MPa}$$

where $\overline{\sigma}$ is the effective stress and $\overline{\varepsilon}$ is the effective strain.

3.2. The Studied Part

A fuel tank part was formed using a two-step deep drawing process. In the first step, forming was performed using a 400 tons single-action press equipped with a die cushion. Both the front and back surfaces of the prepared blank were lubricated uniformly with a press working oil applied using a paint roller. The second step utilized a double-crank 600 tons single-action straight-side mechanical press, primarily to form the sinking region in the end zone. The process was completed with laser trimming to finish the part.

Figure 4a illustrates the punch shapes, representing the final part formed in each step of the process, while Figure 4b shows the zone names on the final part.



(**a**) (**b**)

Figure 4. Illustration of (**a**) shape of punch in first forming (upper) step and second forming step (lower) and (**b**) final part after laser trimming with name of zones.

3.3. Methods

The main procedure comprises three stages.

(1) Material Model Validation (Pre-Study): to validate and select the most accurate material model for the finite element simulation under baseline conditions.
(2) An investigation of a series of process parameters is conducted within the simulation software. For each condition explored in the second stage, the resulting part's formability is evaluated using the Q-value, and the results are analyzed.
(3) The simulated condition that demonstrates the best formability is then selected for experimental validation to confirm the simulation results and the effectiveness of the formability assessment.

3.3.1. Simulation Setup

Forming simulations were conducted using PAM-STAMP v2022.0, utilizing the finite element method (FEM). The IGES CAD file of the tools was imported, and automatic meshing was carried out using the software's meshing tool, DeltaMesh. Adaptive mesh refinement was applied to the blank with a user refinement level of 5. The minimum mesh size was set to 0.9375 mm^2 (calculated as 25% of the sum of the smallest tool's radius (3 mm) and half the blank's nominal initial thickness (1.5 mm): $0.25 \times (3 + 0.5\ (1.5))$). The maximum mesh size was set to 15 mm^2 (corresponding to $2^{\text{refinement level}-1}$ times the minimum size: $2^4 \times 0.9375$). Therefore, mesh sizes ranged from 0.9375 mm^2 to 15 mm^2. The tools were defined as rigid bodies, with all rotational degrees of freedom locked and translational movement restricted in the x and y directions. The Coulomb friction coefficient at the interface between the tools and the blank was set to 0.12. This value was selected based on the recommendations in the software's user guide for lubricated conditions [47] and corresponds to the lubricating oil applied to the blank surfaces, as described in Section 3.2: ("The Studied Part").

Continuous plastic deformation theoretically occurs when the yield function reaches a specified constant. A key mechanical characteristic of sheet metal is its anisotropic behavior, where the material properties vary depending on the direction. In this study, anisotropy was evaluated in the rolling direction (0°), diagonal direction (45°), and transverse direction (90°) in terms of r-values, as shown in Table 1. These r-values were applied to two yield criteria: Hill's 1948 and Barlat and Lian 1989 models [48,49]. The details and findings from the parameter analysis are described in the subsequent sections.

1. Hill's 1948 yield criterion [48]

From the uniaxial tensile test results, a commonly used classical yield criterion is Hill's 1948 yield criterion [48]. This criterion is particularly valuable because it only requires uniaxial tensile test data for determining its model parameters, making it practical and straightforward. Hill's 1948 yield criterion incorporates Lankford's coefficients, which account for anisotropy by using the yield strength in the rolling direction (σ_0). The yield function $f(\sigma_{ij})$ in plane stress can be expressed as shown in Equation (9).

$$f(\sigma_{ij})_{\text{Hill's 1948}} = \overline{\sigma}^{2}_{\text{Hill's 1948}} = (H+G)\ \sigma_{xx}^2 - 2H\ \sigma_{xx}\sigma_{yy} + (H+F)\ \sigma_{yy}^2 + 2N\ \sigma_{xy}^2 \quad (9)$$

where subscripts i and j refer to the x and y directions; similar subscripts indicate normal stresses, while dissimilar subscripts denote shear stress.

The four parameters H, G, N, and F are calculated from formulations given below. And the calculated parameters are listed in Table 2.

$$H = \frac{r_0}{(1+r_0)},\ G = \frac{1}{(1+r_0)},\ N = \frac{(r_0 + r_{90}) \times (2r_{45}+1)}{2 \times (r_{90} + r_0 r_{90})},\ \text{and}\ F = \frac{H}{r_{90}} \quad (10)$$

2. Barlat and Lian 1989 yield criterion [49]

A well-known non-quadratic function models which material's crystallographic properties cause concern by accounting the exponent M.

In 1989, Barlat and Lian [49] published a model that used the stress invariant principle to expand the principal stress into tri-component plane stress. This model defines two parameters, k_1 and k_2, which are functions of stress components including both normal and shear stresses, and involves anisotropic coefficients. The model is formulated as follows:

$$k_1 = \frac{\sigma_{xx} + h\sigma_{yy}}{2} \text{ and } k_2 = \sqrt{\left(\frac{\sigma_{xx} - h\sigma_{yy}}{2}\right)^2 + p^2{\sigma_{xy}}^2} \quad (11)$$

The yield function is then given by:

$$f\left(k_{1,2}(\sigma_{ij})\right)_{\text{Barlat and Lian 1989}} = 2\overline{\sigma}^{M}{}_{\text{Barlat and Lian 1989}} = a|k_1 + k_2|^M + a|k_1 - k_2|^M + c|2k_2|^M \quad (12)$$

The parameters a, c, and h are calculated using the r-values as follows:

$$c = 2 \times \sqrt{\frac{r_0}{1+r_0} \times \frac{r_{90}}{1+r_{90}}}, \quad (13)$$

$$a = 2 - c, \text{ and} \quad (14)$$

$$h = \sqrt{\frac{r_0}{1+r_0} \times \frac{1+r_{90}}{r_{90}}} \quad (15)$$

While finding of the parameter p involves more steps:

$$p = \frac{\sigma_0}{\tau_1} \times \left(\frac{2}{(2a) + (2^M c)}\right)^{1/M} \quad (16)$$

For Equation (16), τ_1 represents the yield strength under pure shear condition, where both were concerned as no σ_{xx} and σ_{yy}. This value is out of conventional uniaxial tensile tests, like the following ASTM E8 specimen.

Table 2. List of parameters for Hill's 1948 and Barlat and Lian 1989 models.

Yield Criteria	Name of Parameters	Values
Hill's 1948 [48]	H	0.36
	G	0.64
	N	1.52
	F	0.53
Barlat and Lian 1989 [49]	M	8.00
	c	0.77
	a	1.23
	h	0.95
	p	1.07

The present work determines the parameter 'p' based on the established relationship between τ_1 and principal stress. This analysis considers the pure shear condition, where σ_{xx} and σ_{yy} are equal to zero. This means that σ_1 is equal to τ_1 and equal to $-\sigma_2$.

Referring to the yield locus in Figure 5, τ_1 is located on the yield locus where it intercepts with the pure shear line. Then, the value of τ_1 was substituted back into the yield function to find the *p* value using the Newton–Raphson iterative solving method with a converged criterion tolerance of 10^{-6} and a maximum number of iterations of 10^{10} times on MATLAB R2023b. Finally, the five parameters in this model were listed in Table 2.

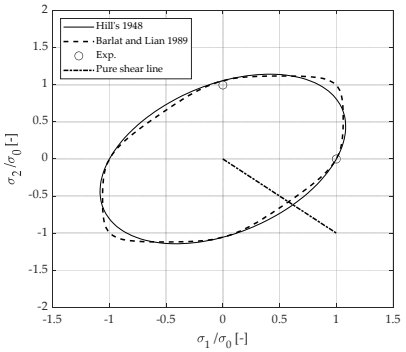


Figure 5. Hill's 1948 [48] and Barlat and Lian 1989 [49] yield loci with pure shear line.

3.3.2. Baseline Condition and Model Validation

The baseline condition consisted of a blank size of 410 mm × 495 mm, a blank holder pressure of 0.8 MPa, and no drawbead cooperation.

For more robust and reliable validation of the simulation models, thickness was the first quantity to be validated. To enhance the density of measurement data for validation, six points were measured in this study using a non-destructive ultrasonic thickness gauge (Dakota Ultrasonics model PVX, Dakota Ultrasonics, CA, USA) with a resolution of 0.01 mm. These measurement points are shown in Figure 6. Additionally, due to wrinkling observed in the side and end zones, a Mitutoyo Digital Micrometer (IP65), Mitutoyo Corporation, Kanagawa, Japan with a ball-head and a resolution of 0.001 mm was used to accurately measure the thickness at the edges of these zones.

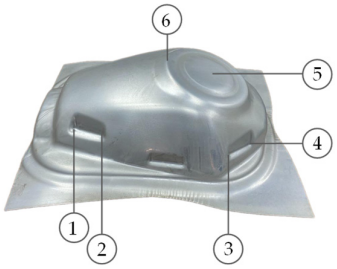


Figure 6. Measurement points for thickness validation (using Ultrasonic Thickness Gauge).

The positions of the six thinning trend points were aligned with their actual locations on the formed part, as defined by the tool constraints in both the simulation and the actual forming process. However, accurate comparison of points in the thickened edge zone is crucial. Therefore, the draw-in distance was measured and compared to ensure sufficient proximity between the simulated and actual positions.

3.3.3. Varying Blank Size Conditions

This investigation examines the effect of varying blank size on the thickness distribution of the final part. Four width increments were studied: 410, 420, 430, and 440 mm. Six length increments were also examined: 490, 495, 505, 515, 525, and 530 mm. Due to concerns about material consumption in the production line, the maximum blank size tested was limited to 440 mm × 530 mm, which represents a 15% increase over the baseline blank size. The 24 test cases are listed in Table 3, where each number represents a unique combination of width and length.

Table 3. Case numbering for blank size variation.

Width [mm] \ Length [mm]	490	495	505	515	525	530
410	1	2	3	4	5	6
420	7	8	9	10	11	12
430	13	14	15	16	17	18
440	19	20	21	22	23	24

3.3.4. Drawbead Shape and Dimensions

Research has explored a wide range of drawbead shapes, including semi-circular, trapezoidal, rectangular, V-shaped, and asymmetrical configurations [50]. Karnchanaseangthong et al. [51] compared the performance of commonly used semi-circular, V-shaped, and trapezoidal drawbeads on a non-symmetrical deep-drawn part under constant blank holder force. Their findings, validated through finite element analysis, highlighted the superior performance of the semi-circular shape in reducing wrinkles and accommodating large metal flow, aligning with its frequent use in industry, as noted by J. Ke et al. [41].

Therefore, this study focuses on the influence of semicircular drawbeads on material flow uniformity. Previous research has extensively studied the impact of drawbead geometries [52], particularly emphasizing that the contra-bead radius and drawbead height significantly affect the restraining force needed to suppress wrinkling. Building upon this, this study investigates the effects of drawbead cross-sectional dimensions. Specifically, it examines variations in male bead height and contra-bead radius (as detailed in Table 4) for drawbeads positioned on the blank holder and upper die, as illustrated in Figure 7.

Table 4. Geometrical dimension of semicircle drawbeads in [mm].

Radius of Male Bead (r)	Width of Groove (W)	Height of Male Bead (H)	Radius of Contra Bead (R)
3	9	2.25	3 4.5 6
		3	3 4.5 6
		3.75	3 4.5 6

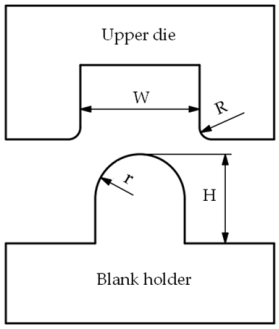


Figure 7. Schematic diagram of semicircle drawbead (R: radius of contra-bead, r: radius of male bead, W: width of groove, and H: height of male bead).

3.3.5. Weight Factor Determination for Formability Assessment

By using thinning limit diagrams with Pascal's triangle coefficients for quantitative evaluation of final part's formability, the methodology employs a severity percentage (*SP*) of 20% and a %Thinning increment (*i*) of 5%, resulting in eleven intervals and n being 10. The lower boundary for thinning is accounted for when the material thickens to 20% and the upper boundary is when the TLC is a function of e_2.

The conditions for determining the weight factor are:

$$W_k = \begin{cases} 1 & \%\ \text{Thinning}(e_2) < 20\% \\ 10 & -20 \leq \%\ \text{Thinning}(e_2) < -15 \\ 45 & -15 \leq \%\ \text{Thinning}(e_2) < -10 \\ 120 & -10 \leq \%\ \text{Thinning}(e_2) < -5 \\ 210 & -5 \leq \%\ \text{Thinning}(e_2) < 0 \\ 252, \text{ when} & 0 \leq \%\ \text{Thinning}\ (e_2) < 0.80(\text{TLC}(e_2)) \\ 210 & 0.80(\text{TLC}(e_2)) \leq \%\ \text{Thinning}\ < 0.85(\text{TLC}(e_2)) \\ 120 & 0.85(\text{TLC}(e_2)) \leq \%\ \text{Thinning}\ < 0.90(\text{TLC}(e_2)) \\ 45 & 0.90(\text{TLC}(e_2)) \leq \%\ \text{Thinning}\ < (0.95\text{TLC}(e_2)) \\ 10 & 0.95(\text{TLC}(e_2)) \leq \%\ \text{Thinning}\ < (\text{TLC}(e_2)) \\ 1 & \text{TLC}(e_2) \leq \%\ \text{Thinning} \end{cases}$$

4. Results and Discussion

4.1. Material's Model Validation

4.1.1. Comparison of Simulation and Experimental Measured Thickness at Baseline Condition

The comparison of the point thickness in six critical thinning regions between two models and the experimental measurements is presented in the bar chart shown in Figure 8. We found that the Barlat and Lian 1989 model gives higher accuracy than Hill's 1948 model for all points [48,49]. The maximum difference occurs at point number 6, between the Barlat and Lian model, where the experimental measurements is 0.05 mm, and Hill's model, where it is 0.143.

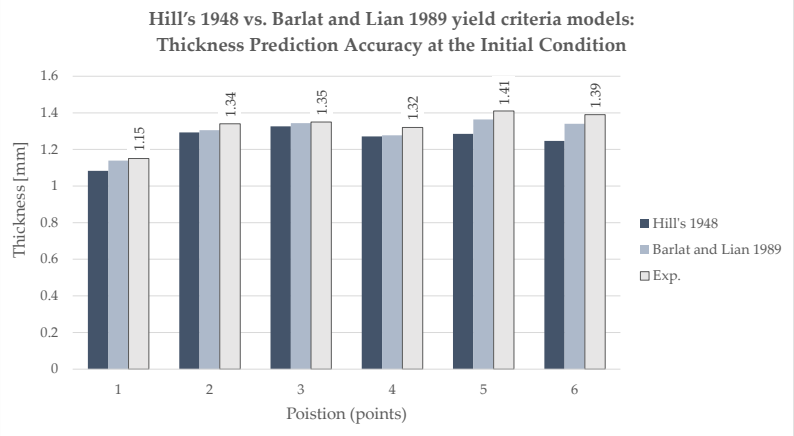
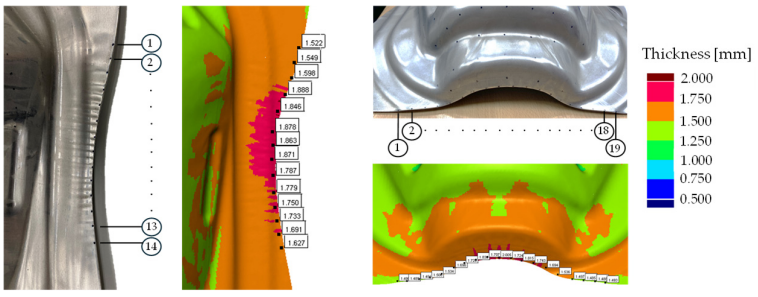


Figure 8. Comparing simulated and measured thickness at six points (using Ultrasonic Thickness Gauge) of the final deep-drawn part in baseline condition [48,49].

For the wrinkling region observed at the edge of the part, additional measurements were taken in the side zone (14 points) and the end zone (19 points) with spaces of 10 mm and 5 mm, respectively, as shown in Figure 9. To support this alignment verification, draw-in values were measured at 12 points on the part (Figure 10). These measurements were compared to draw-in values obtained using a high-accuracy (0.016 mm accuracy) 3D scanner, an 83 series ABSOLUTE ARM (Hexagon Manufacturing Intelligence, RI, USA), adhering to ISO 10360-12 probing accuracy. The resulting values and their relative errors are summarized in Table 5. The data indicate a reliable alignment between the measured and simulated positions, with a maximum relative discrepancy around 9 mm.



(**a**) (**b**)

Figure 9. Measurement positions for thickness distribution in the thickening zones: (**a**) the side zone; and (**b**) the end zones of final deep-drawn part under baseline condition (using Micrometer).

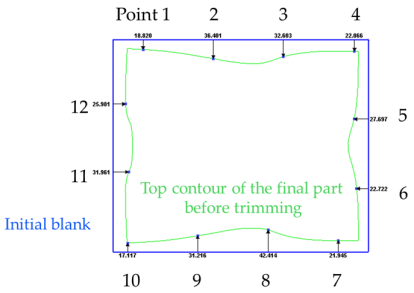


Figure 10. Twelve points on the contour curve of final deep-drawn part's top view for comparing draw-in values.

Table 5. Draw-in value for 12 points and relative error between simulated and experimental results.

Position (Points)		1	2	3	4	5	6	7	8	9	10	11	12
Draw-in value [mm]	Exp.	21.93	29.14	23.60	20.17	31.02	21.79	25.64	40.63	27.36	16.87	33.67	28.33
	Simulation	18.82	36.40	32.60	22.07	27.70	22.72	21.95	42.41	31.22	17.12	31.96	25.98
Relative error [mm]		3.11	3.11	7.26	9.00	1.90	3.33	0.93	3.70	1.79	3.86	0.25	1.71

The measured thicknesses from the simulated and actual parts for both the side zone and end zone are shown in Figure 11. In the side zone, the mean absolute error between simulated and actual thicknesses was 0.123 mm for Hill's 1948 model and 0.125 mm for the Barlat and Lian 1989 model [48,49]. For the end zone, the average absolute differences were 0.145 mm and 0.150 mm for Hill's model and the Barlat and Lian model, respectively.

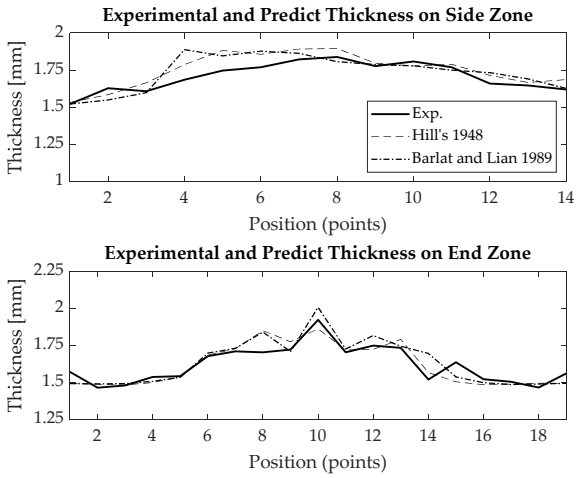


Figure 11. Experimental (using Micrometer) and predicted thickness by Hill's 1948 [48] and Barlat and Lian 1989 [49] on side zone and end zone of the final deep-drawn part in baseline condition.

4.1.2. Accuracy of Formability Prediction Using the Thinning Limit Diagram

Section 4.1.1 examined the part's thickness in its dominant thinning and thickening regions before trimming. The validation analysis led to the selection of the Barlat and Lian 1989 model [49] for further investigation.

Continuing the present section, the thinning limit diagram (TLD) utilizes strain paths based on the Barlat and Lian 1989 model. The TLD incorporates the boundary curve of the necking limit (also referred to as the thinning limit curve in this study), which is derived from the strain-approach forming limit curve (ε-FLC) plot obtained from Nakajima test information [53]. This ε-FLC has already been shown to predict cracking phenomena accurately in the same studied material.

The ability to identify wrinkling regions is demonstrated by comparing the visually identified wrinkles on the actual part with those predicted by the thinning limit diagram.

This diagram establishes a basic wrinkle boundary based on the occurrence of thickening (where % thinning is less than 0), as shown in Figure 12. Figure 12 presents the thinning limit diagram for the final deep-drawn part in its baseline condition. The purple-colored region in the diagram, as indicated in the legend, represents the wrinkling trend zone. Wrinkles on the physical part, highlighted by rectangular boxes (top of Figure 12), align visually with the purple zone on the simulated part (bottom left of Figure 12), where color is shown in accordance with the legend of the thinning limit diagram.

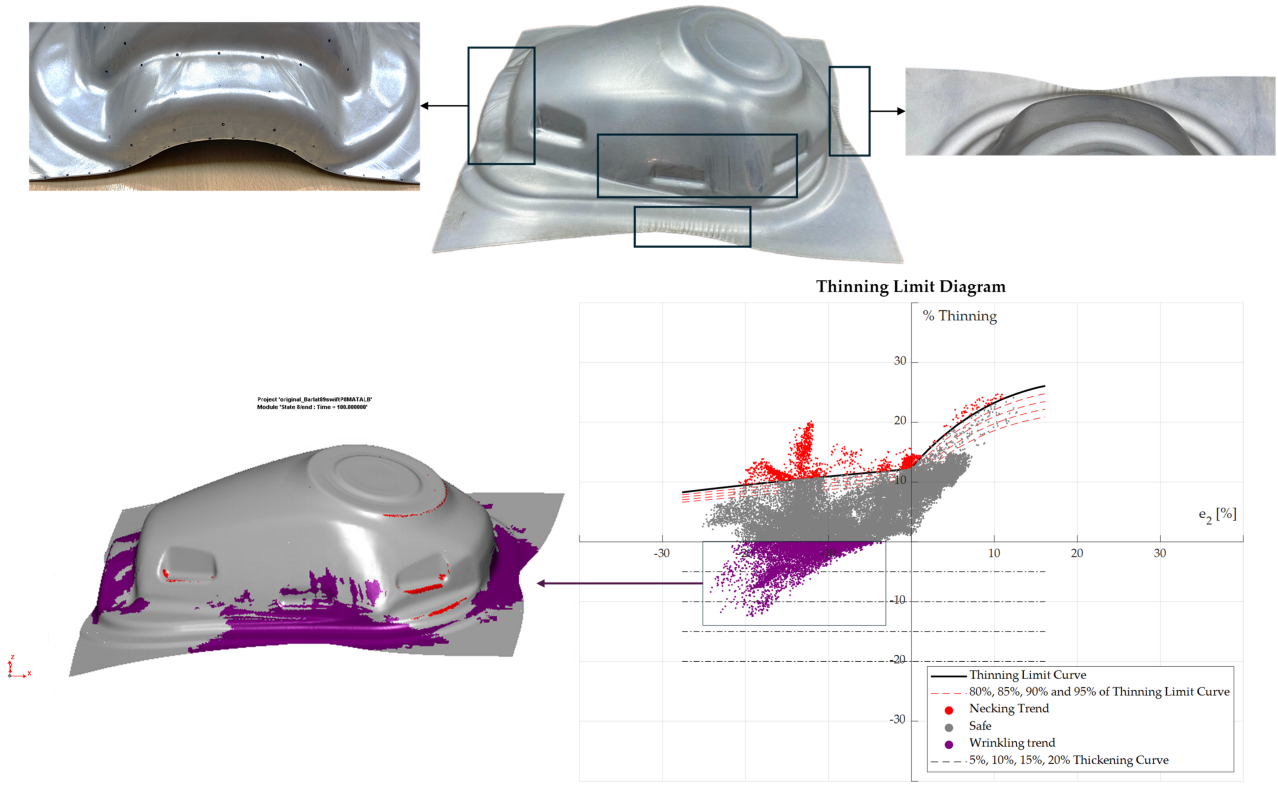


Figure 12. Thinning limit diagram for final deep-drawn part in baseline condition.

4.2. Influence of Blank's Length and Width on Distribution of Thickness and Q-Value

The influence of varying initial blank dimensions on thickness distribution of the deep-drawn part before trimming is evident in Figure 13. This figure is not intended to directly evaluate the quality of the final trimmed part in terms of wrinkling and necking but rather to visualize trends in thickness distribution. These trends provide valuable insights into how blank size influences thickening and thinning phenomena, which are precursors to wrinkling and necking, respectively, across the entire part (both inside and outside the trimline). This preliminary analysis serves to complement the comprehensive formability evaluation of the final trimmed part, which is quantified using the Q-value derived from the thinning limit diagram.

Observations and analyses of Figure 13 reveal distinct trends in thickness distribution within the end and side zones. Regions with higher thickness than the original blank thickness (1.5 mm) are represented by yellow and warmer colors in the provided range. In the side zone, increasing the blank length while keeping the width constant results in more pronounced thickening. Conversely, increasing the width while keeping the length constant relieves thickening in this zone. In the end zone, thickening becomes more pronounced as the width increases, regardless of length variation. Conversely, increasing the blank length reduces thickening in this zone.

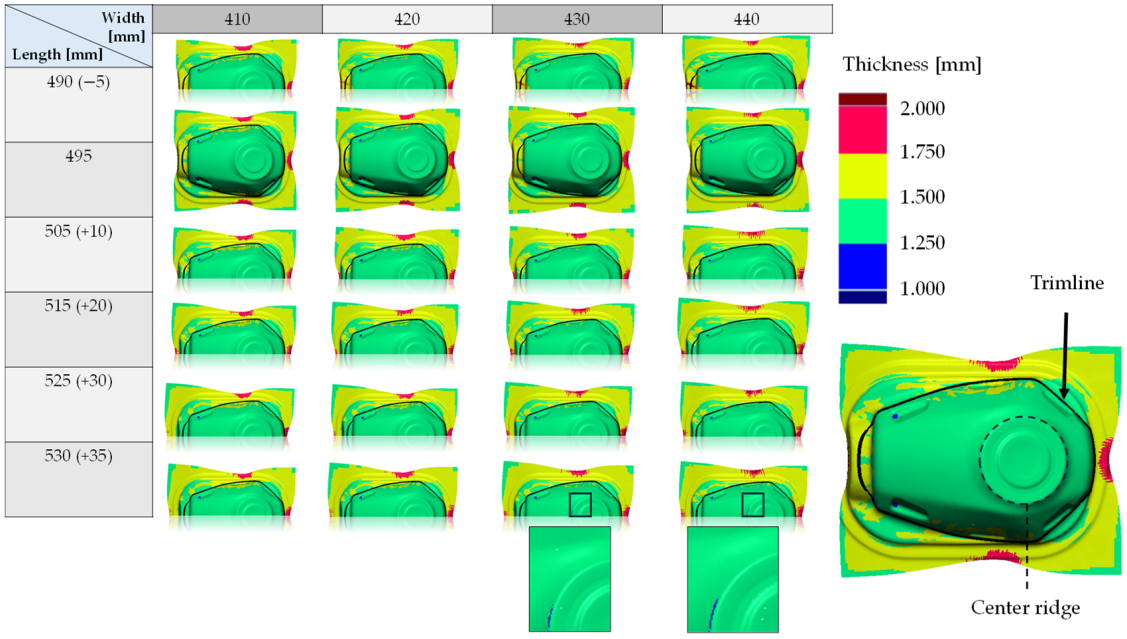


Figure 13. Influence of initial blank dimensions on deep-drawn part's thickness distribution before trimming.

The observations suggest that the blank holder force plays a significant role in influencing thickness distribution. Both increasing length and width result in a larger contact area between the blank and the blank holder. This increased contact area, under constant blank holder pressure, leads to higher holding force, which effectively suppresses thickening [54].

However, the effect of increasing both length and width on the final trimmed part is more complex. Increasing both dimensions beyond a specific limit, particularly when length exceeds 530 mm and width exceeds 430 mm, appears to result in pronounced thinning (indicated by the blue regions in Figure 14, representing thicknesses less than 1.25 mm) on the center ridge of the trimmed part. Furthermore, although the increased area of the blank is the highest for both dimensions for 440 mm width and 530 mm length (the area is 15% greater than the original), the wrinkling trend in the side zone remains dominant, as predicted by the thinning limit diagram in Figure 14.

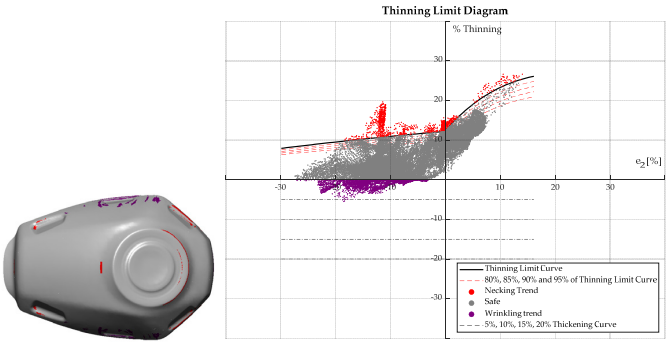


Figure 14. Thinning limit diagram for final trimmed part (440 mm × 530 mm blank, original tool).

Following the observations of thickness distribution for each combination of blank width and length, the influence of these parameters on formability was further analyzed using the Q-value. Figure 15 presents an interaction plot illustrating their combined effect. The non-parallel and intersecting lines, particularly those representing width variation across different lengths, demonstrate a clear interaction between these parameters.

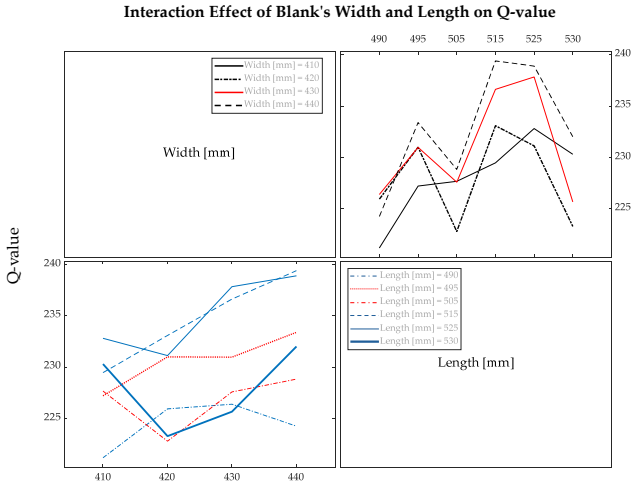


Figure 15. Interaction plot of blank's width and length on Q-value.

While varying the length within each width (410, 420, 430, and 440 mm) gives quite similar Q-value trends, the non-parallelism and intersections of curves confirm the interaction. This aligns with the thickness distribution analysis, which clearly showed that increasing width at a constant length reduces thickening in the side zone.

Optimal blank dimensions, maximizing formability (corresponding to Figure 15's highest Q-value), are 440 mm width and 515 mm length. Figure 16b shows the TLD for this optimal case compared to the baseline condition in Figure 16a, demonstrating a visible improvement. This improvement is further highlighted when compared to the non-optimal blank size (440 mm × 530 mm) shown in Figure 13, reinforcing the effectiveness of the Q-value for formability assessment.

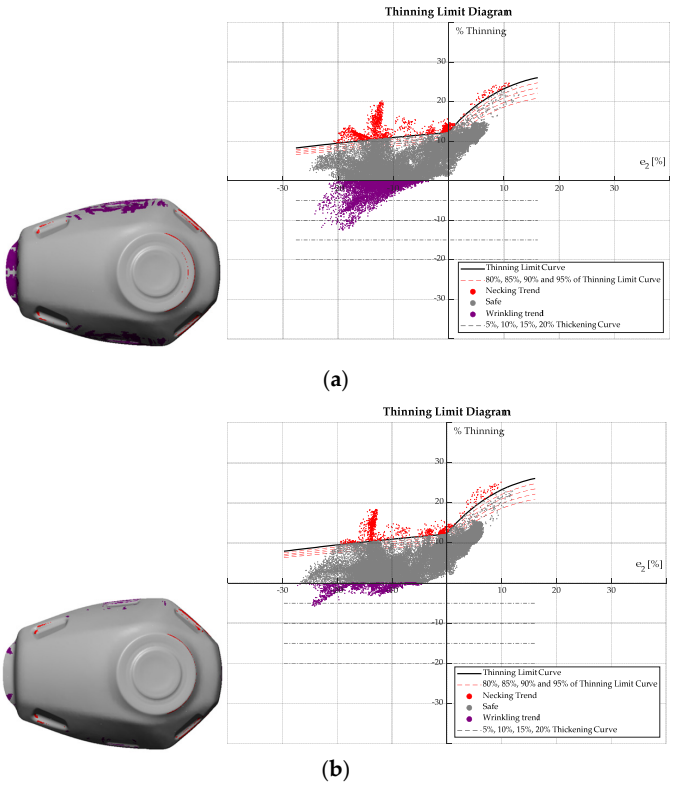


Figure 16. Thinning limit diagrams for trimmed part of (**a**) baseline condition 410 mm × 495 mm blank and (**b**) 440 mm × 515 mm blank.

After optimizing blank dimensions based on the Q-value, Figure 16b shows the region that is prone to wrinkling (purple zone) is visibly smaller when compared to the baseline condition in Figure 16a. However, wrinkles are still present in the side and end zones. Similarly, the necking-prone region is reduced compared to the baseline but persists, especially in the head zone near the sinking corner. Thus, while the optimal blank size improves formability, it does not fully eliminate wrinkling and necking.

4.3. Side-Wall Wrinkle Formation: Cause Analysis and Evaluation of Proposed Solutions

4.3.1. Cause Analysis and Proposed Solution (Tools Redesign)

To address the wrinkling problem, the baseline blank size, which exhibited the most severe wrinkling, was selected for analysis. Figure 12 shows distinct side-wall wrinkles (non-flange wrinkles), located solely in the side zone and unconnected to the flange wrinkles. A finite element analysis (FEA), simulating both deep drawing operations, was performed to investigate the origin of these side-wall wrinkles.

The FEA revealed that the side-wall wrinkle first forms during the first deep drawing operation. The wrinkles were observed after the upper die and the blank holder made contact, and the blank moved downward 15 mm before reaching the end of the stroke, as highlighted in Figure 17. This indicates that the wrinkle develops after the flange region has been already passed over the die radius.

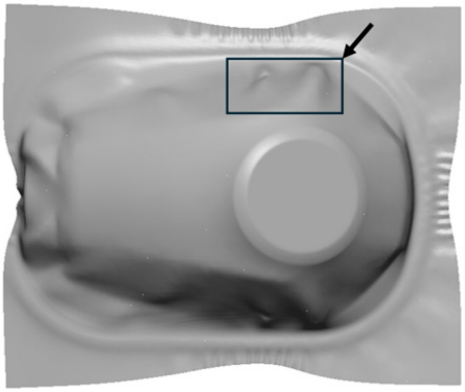


Figure 17. FEA results illustrating initial side-wall wrinkle formation (first deep drawing operation, upper die position: 15 mm before end of stroke) for 410 mm × 495 mm blank.

Tracing back to 45 mm before the end of the stroke (Figure 18) reveals a crucial factor: the side-wall region lacks tool support. Figure 18a shows a side view of the deformed blank and tools during the forming process. The regions of the deformed blank that lacks support from the upper die are pointed out, with the die shown transparently for clarity in Figure 18b, and the lack of support from the punch was pointed in Figure 18c (the blank is shown transparently, and the die is hidden for easy visualization).

The lack of support creates a unique stress distribution that contributes to wrinkle formation. Analyzing the principal stresses (Figure 19) reveals further insights. The protruding portion of the upper die, designed for forming the sinking region, generates tension and acts as a "locker" trapping the material, first in the head zone and then in the side zone, according to the tool design specific to the part. Simultaneously, the unsupported region between the sinking corners experiences increasing contact pressure from both the upper die and lower punch as the die moves downward. This pressure causes the material to fold, leading to wave formation in the unsupported area, ultimately resulting in side-wall wrinkling.

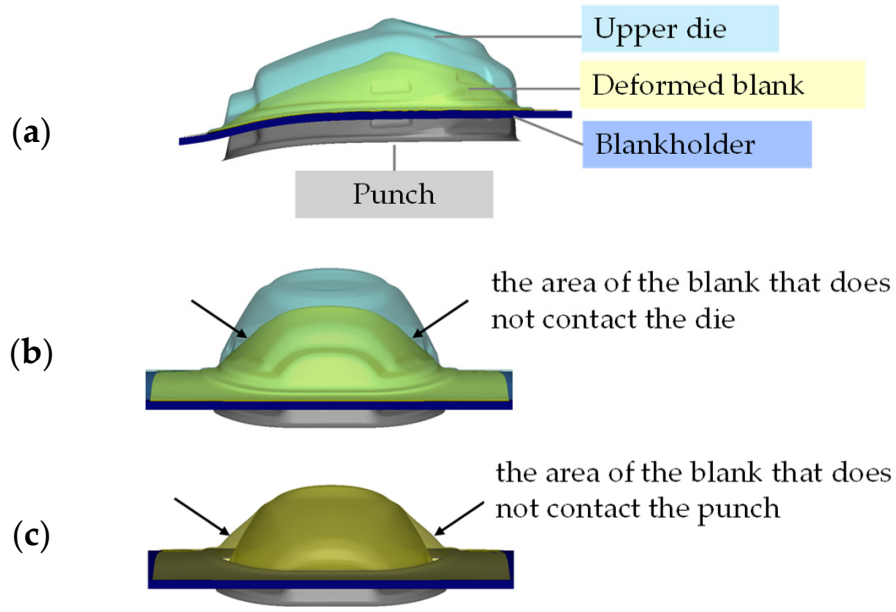


Figure 18. First operation of deep drawing process for 410 mm × 495 mm blank at 45 mm before end of the stroke: (**a**) side view; (**b**) front view—side-wall region unsupported by upper die (transparent die); and (**c**) front view—side-wall region unsupported by punch (transparent blank).

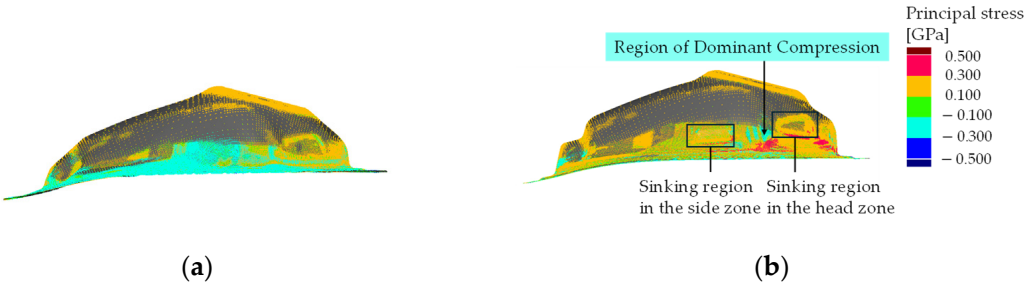


Figure 19. Principal stress distribution during the first operation of deep drawing for 410 mm × 495 mm blank (**a**) 15 mm before end of the stroke and (**b**) at end of the stroke.

The side-wall wrinkling phenomenon described above is known as puckering [55]. It is a type of wave formation on the wall of a drawn shape that occurs after the material has passed over the die radius, and the severity of puckering is mentioned to increase with the size of the blank area that lacks tool support during forming [56].

The stress distribution analysis indicates that the side-wall wrinkle, or puckering, arises primarily from the die's geometry, specifically the lack of tool support in the side-wall region. Rather than this, the red zone shown in Figure 19b suggests that the bent edges cause obstructed flow of the blank during forming due to representing high tensile stress. For this reason, to address the issue of puckering and difficulty of flow during the deep drawing process, which leads to excessive thinning and necking, a new design for the first operation tool was developed, as illustrated in Figure 20. The new design increases the area where the tool supports the blank during forming and removes two protruding regions and the bent edges, which were identified as hindering the blank's flow. Note: for reasons of confidentiality, dimensions are not included in the figure.

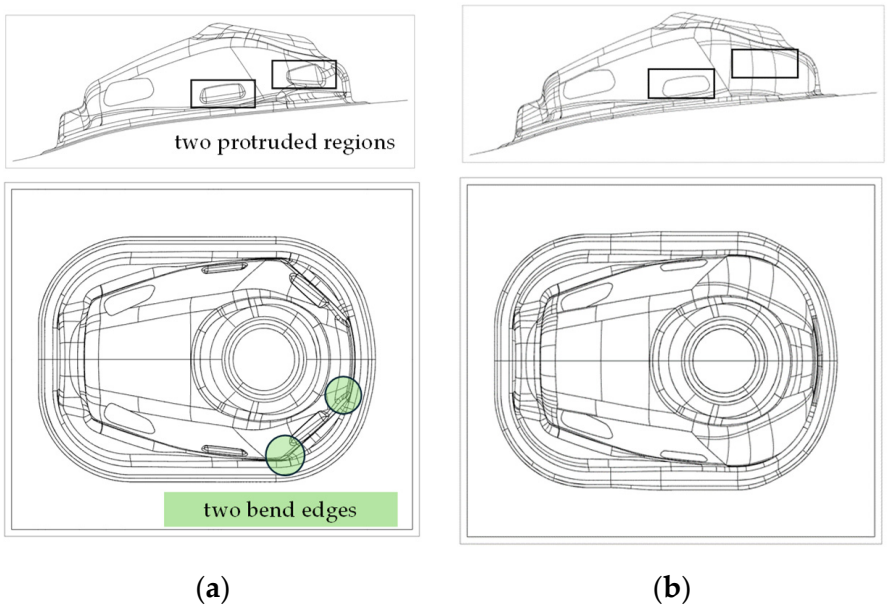


Figure 20. Comparison of (**a**) previous and (**b**) newly designed die for the first operation tool.

4.3.2. Effectiveness of Redesigned Tool Through Q-Values Analysis

Redesigning the first deep drawing operation tool and incorporating variations in the initial blank's length and width led to a substantial improvement in formability, as quantified by the Q-value. Figure 21 clearly illustrates this enhancement, demonstrating that the new tool consistently achieves higher Q-values compared to the original tool for identical blank dimensions.

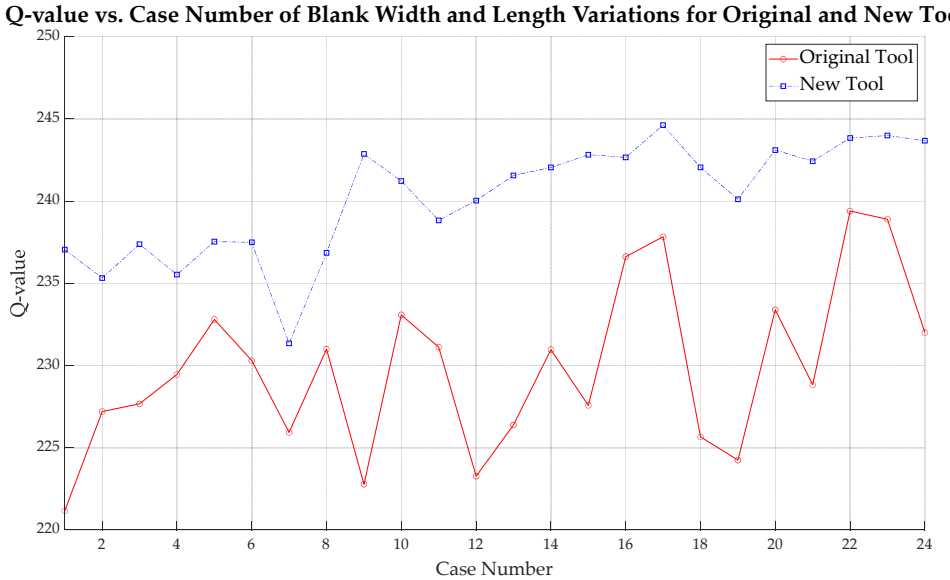


Figure 21. Q-value versus initial blank's size variation for original and new tools.

Furthermore, comparing the formed part using the new tool with a 440 × 515 mm blank (the optimal size identified in Section 4.2) (Figure 22) to a part of the same blank size formed with the original tool (Figure 16b) reveals a reduction in side-wall wrinkles and, importantly, a decrease in thinning in the sinking corner's head zone. So, the effectiveness of the tool redesign is confirmed.

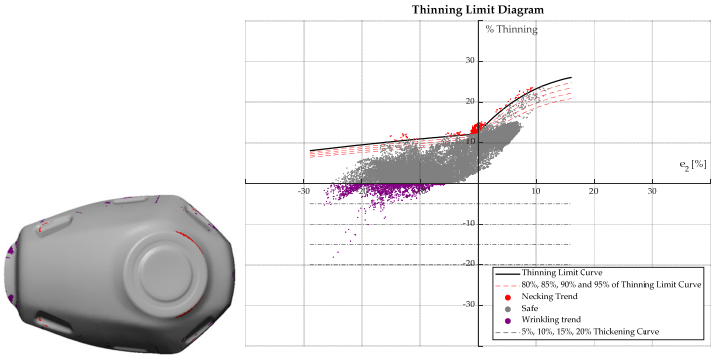


Figure 22. Thinning limit diagram for trimmed part (440 mm × 515 mm blank, new tool).

The optimal blank size for the new tool that gives the highest Q-value in Figure 21 is the 17th case (430 mm × 525 mm blank). The corresponding TLD and formed part are shown in Figure 23. Visually comparing the TLD for this optimal case to the TLD for the previous optimal blank size (Figure 22) offers a limited ability to assess which one exhibits better formability. Similarly, the forming limit diagram (FLD) (Figure 24), a traditional formability assessment tool, is also limited in this aspect. This difficulty arises because of the little difference in formability between cases, and the varying mesh densities used in the simulations, leading to variations in the total number of elements. Consequently, slight differences in the TLD and FLD between cases may not be reliably interpreted.

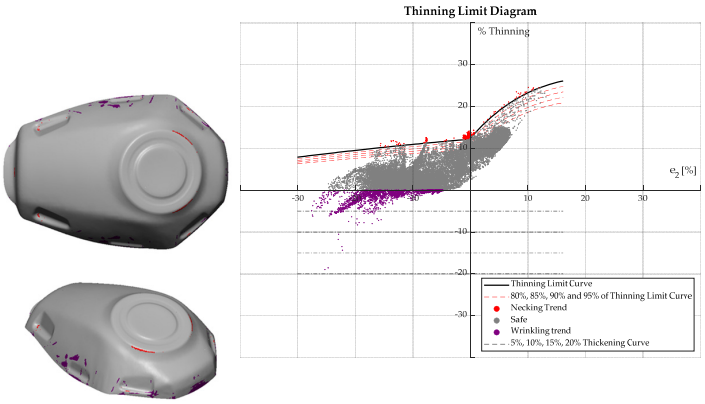
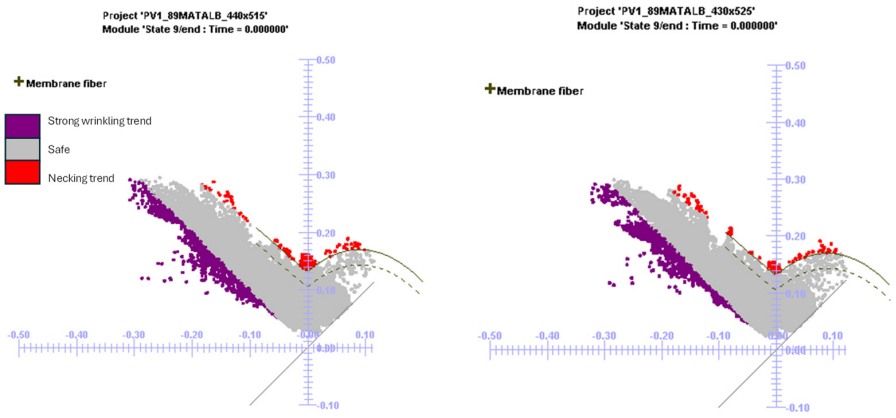


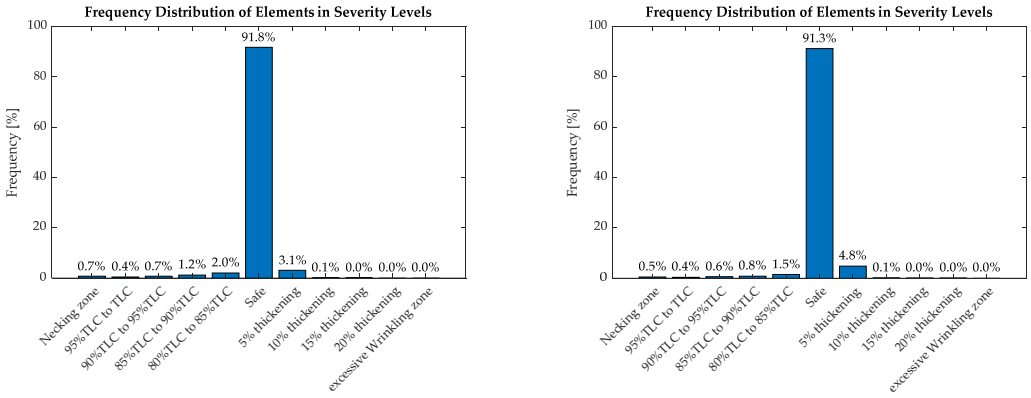
Figure 23. Thinning limit diagram for trimmed part (430 mm × 525 mm blank, new tool).



(**a**) (**b**)

Figure 24. Strain-based forming limit diagrams for trimmed part of (**a**) 440 mm × 515 mm blank (new tool) and (**b**) 430 mm × 525 mm blank (new tool).

However, this study's novel assessment method addresses this issue by normalizing the severity within each interval based on the ratio of elements to the total number and applying a weighting factor. This normalization enables direct comparison of results across different simulations. Regarding the comparison of the 440 × 515 mm (new tool) and 430 × 525 mm (new tool, optimal condition) blanks, the bar chart of normalized frequencies (Figure 25) supports this assessment. The optimal case shows a lower frequency of thinning issues on the left side of the chart for all levels of thinning, despite a slightly higher frequency in the 5% thickening interval, but this is the first severity level in thickening (besides the safe zone bar). Thus, this novel Q-value assessment considers both the severity of necking/wrinkling and the normalized volume (frequency), making it a robust tool for comparing the formability of simulations.



(**a**) (**b**)

Figure 25. Frequency distribution of elements in severity levels for (**a**) 440 mm × 515 mm blank (new tool) and (**b**) 430 mm × 525 mm blank (new tool).

4.4. Influence of Male Bead Height and Contra-Bead Radii on the Formability of the Part

Based on the optimum condition identified from the Q-value analysis in Section 4.3.2, a 430 mm × 525 mm blank was formed by using the new tool. The frequency distribution of elements across different severity levels, as shown in Figure 25, reveals that thickening persists for 5% of the total number of elements. This is the second major portion and is related to the wrinkling zone (purple color shown in the head and side zones of the part). To investigate the persistent thickening in the final trimmed part, the analysis shifted to the pre-trimming stage. As shown in Figure 26, a concave region is observed on the flange, primarily in the area where thickening is most prominent. Empirical observations suggest that material flow is enhanced in this concave region compared to adjacent areas, leading to the decision to incorporate drawbeads.

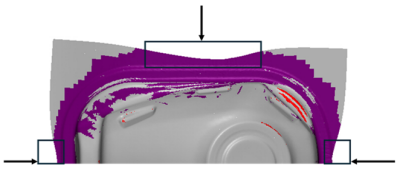


Figure 26. Flange concavity at pre-trimming stage (430 mm × 525 mm blank, new tool).

Drawbeads, with specific dimensions detailed in Table 4, were integrated into the first operation tool. Each drawbead had a length of 120 mm for both the head and end zones and 165 mm for both side zones. A 20 mm open curve section was incorporated at the end of each drawbead. The positioning of the drawbeads on the upper die is illustrated in

Figure 27. Note that due to the confidentiality of the part's dimensions, only the relevant dimensions for drawbead placement are displayed.

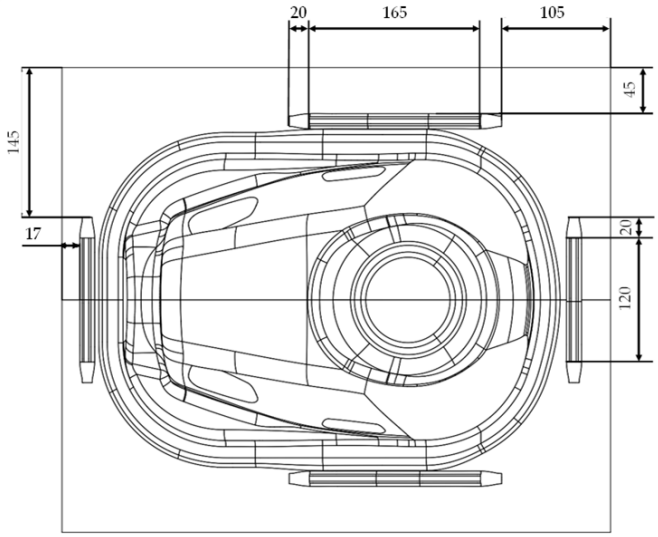


Figure 27. Schematic of drawbeads' layout on the upper die (new tool) in [mm].

Figure 28 shows that a male bead height of 2.25 mm and a contra-bead radius of 3 mm yield the highest Q-value of 244.70, as depicted in the thinning limit diagram and the simulated part in Figure 29a. This value slightly exceeds even the highest Q-value of 244.62 observed for the new tool (without a drawbead) in Figure 23. This comparison demonstrates that adding a drawbead effectively suppresses wrinkling (in the side, head, and end zones), although it does lead to slightly increased thinning.

The influence of the contra-bead radius and male bead height on the Q-value reveals that increased male bead heights negatively impact formability, resulting in lower Q-values. Conversely, a larger contra-bead radius generally enhances formability due to a decrease in drawbead restraining force (DBRF) with increasing radius [41,57]. However, this positive effect on formability plateaus beyond a certain radius.

Interestingly, the impact of the contra-bead radius differs when using a smaller male bead height of 2.25 mm. To further investigate the factors affecting formability in this scenario, thinning limit diagrams (TLDs) were examined for a 2.25 mm male bead height with contra-bead radii of 3 mm and 6 mm, as shown in Figure 29a,b, respectively. The figures reveal that the red zone (indicating trend of necking) on the second quadrant (top-left red zones) of the thinning limit diagram in Figure 29a is noticeably smaller than in Figure 29b, and the purple zone (representing thickening) also exhibits slight variations.

To highlight the second quadrant, the corresponding areas on the formed parts are indicated in black in Figure 30. These indicated regions demonstrate that a contra-bead radius of 6 mm results in a larger affected area compared to the 3 mm radius. Examination of the pre-trimmed stage at the end of the stroke (Figure 31) reveals wrinkles in the flange area's side zone for the 6 mm contra-bead radius case. Principal stress analysis indicates that wrinkling occurs around the protruding bead in this case, with the region experiencing predominantly high tensile stress compared to the 3 mm contra-bead radius case. Especially, the area that is parallel to the bead and extending inward towards the part's center experiences predominantly higher tensile stress compared to the 3 mm contra-bead radius case.

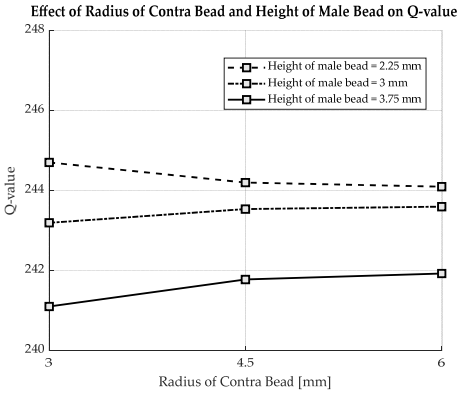
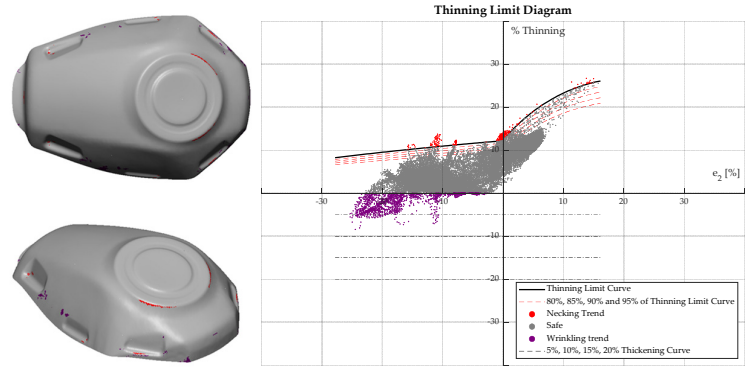
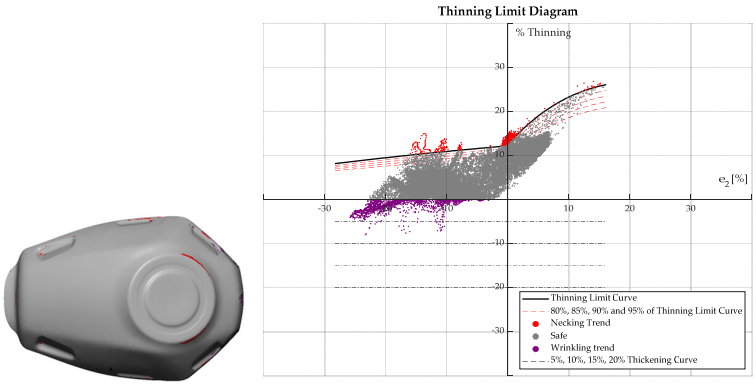


Figure 28. Q-value variation with contra-bead radius for different male bead heights.



(**a**)



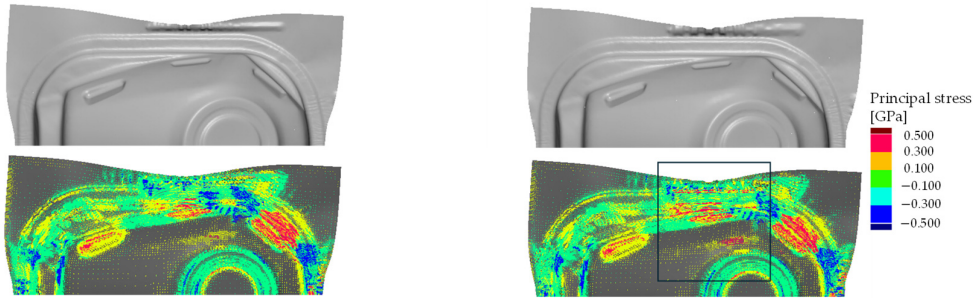
(**b**)

Figure 29. Thinning limit diagrams for trimmed part (430 mm × 525 mm blank, new tool with 2.25 mm male bead height drawbead) with contra-bead radii of (**a**) 3 mm and (**b**) 6 mm.



(**a**) (**b**)

Figure 30. Trimmed parts with critical thinning zones highlighted (black region): (**a**) 3 mm contra-bead radius; and (**b**) 6 mm contra-bead radius (in 430 mm × 525 mm blank, new tool with 2.25 mm male bead height drawbead).



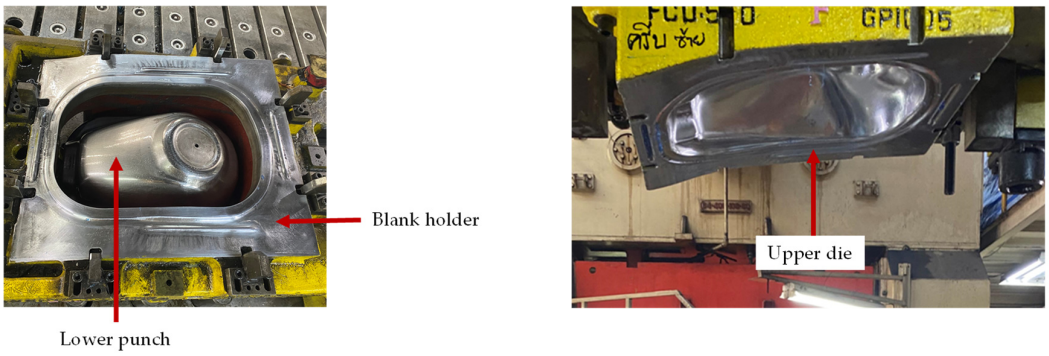
(**a**) (**b**)

Figure 31. Pre-trimmed blank at end of stroke and principal stress distribution (in 430 mm × 525 mm blank, new tool with 2.25 mm male bead height drawbead): (**a**) 3 mm contra-bead radius and (**b**) 6 mm contra-bead radius.

These findings suggest that a larger contra-bead radius provides less restraining force from the drawbead, allowing material to flow more easily. This increased material flow, coupled with the low male bead height, which also facilitates flow, results in insufficient suppression of wrinkling and leads to severe thinning, similar to the observations made in the case of insufficient blank holder force discussed in Section 4.2.

4.5. Validation of Enhanced Formability Achieved Through Q-Value Analysis

Based on finite element simulations, which guided the experimental design, the formability of the final part was enhanced by modifying the blank size, redesigning the first operation tools, and incorporating drawbeads into the new tool design for controlling material flow. The optimal configuration, determined through Q-value analysis, involved a blank size of 430 mm × 525 mm formed using a tool with drawbeads featuring a male bead height of 2.25 mm and a contra-bead radius of 3 mm. To validate these simulation-derived parameters, a physical tool was fabricated and set up on the press, as shown in Figure 32.



(**a**) (**b**)

Figure 32. Experimental setup: First deep drawing operation tools fabricated based on simulation-optimized design—(**a**) lower tool and (**b**) upper tool.

The resulting part from the deep drawing operations is displayed in Figure 33. Wrinkling in the side wall and end zones, previously observed in the baseline condition (Figure 12), has been successfully eliminated. This improvement aligns with the simulation results illustrated in Figure 29a, which also demonstrate the absence of wrinkling in the side and end zone. Regarding the thinning zone, both practical observations and simulation results consistently indicate critical areas in the center ridge and the corners of the sucking region.

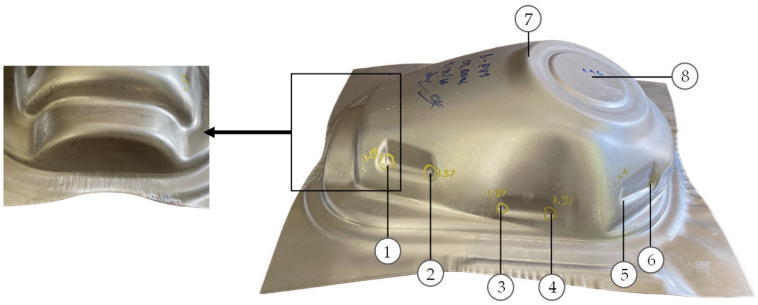


Figure 33. Final deep-drawn part and measurement points for thickness validation (using Ultrasonic Thickness Gauge) in optimized condition.

To validate the improved formability achieved, the thickness profile was measured using the same methodology described in Section 3.3.2 ("Baseline Condition and Model Validation") at specific locations indicated in Figure 33. Table 6 compares the thickness values in these critical regions, validating the observed improvements with a maximum percentage error of 3.65%.

Table 6. Comparing simulated and measured thickness at eight points (using Ultrasonic Thickness Gauge) of the final deep-drawn part in optimized conditions.

Position (Points)		1	2	3	4	5	6	7	8
Thickness value [mm]	Exp.	1.15	1.37	1.37	1.31	1.39	1.46	1.34	1.46
	Simulation	1.12	1.32	1.36	1.34	1.39	1.41	1.30	1.42
Absolute percentage error [%]		2.61	3.65	0.66	2.21	0.36	3.22	3.21	2.74

5. Conclusions

This research establishes a Q-value-based formability assessment. The Q-value, derived from thinning limit diagrams (TLDs), utilizes severity levels defined by offsets from thinning and wrinkling limit curves. It is calculated by summing the product of a Pascal's coefficient weighting factor and the normalized number of elements within each severity interval (the ratio of elements in each interval to the total number of elements).

The effectiveness of the Q-value assessment was demonstrated by optimizing parameters in a deep-drawing process using finite element analysis (FEA). These parameters included blank size, tool design, and drawbead geometry. The accuracy of FEA results using both Hill's 1948 and the Barlat and Lian 1989 yield criteria was validated against experimental thickness distribution measurements for the baseline (pre-study) condition [48,49]. Both criteria provided accurate thickness predictions, with the Barlat and Lian 1989 model demonstrating superior accuracy and therefore being selected for subsequent parameter optimization.

Analysis of the blank's width and length variations revealed an interaction between these dimensions and their influence on formability, a finding corroborated by thickness distribution analysis. Tool geometry was then redesigned based on FEA principal stress analysis, which highlighted flow restrictions caused by bent edges and protruding die regions. Furthermore, the analysis identified the cause of side-wall wrinkling (puckering) as insufficient blank support during forming. The redesigned tool increased supporting surface area, effectively reducing thinning and wrinkling, although some wrinkling persisted in the side and head zones. To address this, drawbeads were incorporated, and their geometry (male bead height and contra-bead radius) was varied. Increased male bead height induced localized thinning, while a larger contra-bead radius facilitated material flow and improved the Q-value. However, an excessively large contra-bead radius proved ineffective in suppressing wrinkles and even exacerbated thinning. An optimal drawbead geometry of 2.25 mm male bead height and 3 mm contra-bead radius effectively reduced wrinkling while only slightly increasing thinning.

Through this optimization process, an optimal configuration was determined as 430 mm × 525 mm blank size, which, combined with the redesigned tool and optimized drawbeads, achieved higher formability with minimized wrinkling and thinning. The Q-value method shown overcomes limitations of traditional forming limit diagrams (FLDs), which are challenged by visually minor differences and are sensitive to differing element counts across simulations. The Q-value's normalization, using the ratio of elements in each severity interval to the total element count, provides a consistent and readily interpretable metric for assessing formability improvements, even for slight variations. Hence, this Q-value-based assessment offers valuable insights for optimizing deep-drawing processes, leading to enhanced product quality and reduced manufacturing defects.

Author Contributions: Conceptualization, J.L., A.S. and S.S.; methodology, J.L.; software, J.L. and A.S.; validation, J.L.; formal analysis, J.L.; investigation, J.L.; resources, J.L.; data curation, J.L.; writing—original draft preparation, J.L.; writing—review and editing, J.L., A.S. and S.S.; visualization, J.L., A.S. and S.S.; supervision, S.S.; project administration, S.S.; funding acquisition, J.L. and S.S. All authors have read and agreed to the published version of the manuscript.

Funding: This research was funded by the Petchra Pra Jom Klao Ph.D. Research Scholarship from King Mongkut's University of Technology Thonburi.

Data Availability Statement: The raw data supporting the conclusions of this article will be made available by the authors on request.

Acknowledgments: The authors gratefully acknowledge the R&D and production planning departments of Thai Summit Gold Press Co., Ltd. for their kind support in materials and resources for the experiment. The authors also sincerely thank King Mongkut's University of Technology Thonburi for the financial support provided through the Petchra Pra Jom Klao Ph.D. Research Scholarship.

Conflicts of Interest: The authors declare no conflict of interest.

References

1. Colgan, M.; Monaghan, J. Deep Drawing Process: Analysis and Experiment. *J. Mater. Process Technol.* **2003**, *132*, 35–41. [CrossRef]
2. Jain, M.; Allin, J.; Bull, M.J. Deep Drawing Characteristics of Automotive Aluminum Alloys. *Mater. Sci. Eng. A* **1998**, *256*, 69–82. [CrossRef]
3. Ghouati, O.; Gelin, J.-C.; Lenoir, H. Process Optimisation in Deep Drawing. *Rev. Eur. Éléments Finis* **2000**, *9*, 129–149. [CrossRef]
4. Devendar, G.; Reddy, A.C. Study on Deep Drawing Process Parameters-A Review. *Int. J. Sci. Eng. Res.* **2016**, *7*, 149–155.
5. Li, S. Sheet Metal Deep Drawing for Making Metallic Parts and Structures. In *Encyclopedia of Materials: Metals and Alloys*; Caballero, F.G., Ed.; Elsevier: Oxford, UK, 2022; pp. 182–196. ISBN 978-0-12-819733-2.
6. Leu, D.-K. The Limiting Drawing Ratio for Plastic Instability of the Cup-Drawing Process. *J. Mater. Process Technol.* **1999**, *86*, 168–176. [CrossRef]
7. Demirci, H.I.; Yaşar, M.; Demiray, K.; Karalı, M. The Theoretical and Experimental Investigation of Blank Holder Forces Plate Effect in Deep Drawing Process of AL 1050 Material. *Mater. Des.* **2008**, *29*, 526–532. [CrossRef]
8. Choudhari, C.S.; Khasbage, S.S. Experimental Investigation of Forming Parameters for Square Cup Deep Drawing Process. *Mater. Today Proc.* **2021**, *44*, 4261–4267. [CrossRef]
9. de Jesu´s Garci´a Zugasti, P.; Medelli´n Castillo, H.I.; de Lange, D.F. A Case Study of Drawbead Design of a Deep Drawn Rectangular Part Using FEM. In Proceedings of the ASME International Mechanical Engineering Congress and Exposition, Lake Buena Vista, FL, USA, 13–19 November 2009; Volume 43772, pp. 21–26.
10. Chen, F.-K.; Chiang, B. Three-Dimensional Finite Element Analysis for the Stamping of a Motorcycle Oil Tank. *J. Manuf. Sci. Eng.* **1998**, *120*, 770–773. [CrossRef]
11. Khuanngern, B.; Suranuntchai, S. Analysis and Correction of Defects for Deep Drawing Process of Stainless Sink by Use of Finite Element Simulation. *Key Eng. Mater.* **2021**, *889*, 153–159. [CrossRef]
12. Wang, H.; Yan, Y.; Han, F.; Wan, M. Experimental and Theoretical Investigations of the Forming Limit of 5754O Aluminum Alloy Sheet under Different Combined Loading Paths. *Int. J. Mech. Sci.* **2017**, *133*, 147–166. [CrossRef]
13. Sun, L.; Cai, Z.; He, D.; Li, L. Aluminum Alloy Sheet-Forming Limit Curve Prediction Based on Original Measured Stress–Strain Data and Its Application in Stretch-Forming Process. *Metals* **2019**, *9*, 1129. [CrossRef]

14. Li, X.; Chen, Y.; Lang, L.; Xiao, R. A Modified M-k Method for Accurate Prediction of Flc of Aluminum Alloy. *Metals* **2021**, *11*, 394. [CrossRef]
15. Ma, B.; Yang, C.; Wu, X.; Zhan, L. Theoretical and Numerical Investigation of the Limit Strain of a 5754-O Aluminum Alloy Sheet Considering the Influence of the Hardening Law. *J. Mater. Eng. Perform.* **2023**, *32*, 10115–10127. [CrossRef]
16. Butuc, M.C.; Gracio, J.J.; Barata da Rocha, A. A Theoretical Study on Forming Limit Diagrams Prediction. *J. Mater. Process Technol.* **2003**, *142*, 714–724. [CrossRef]
17. Bunyan, T.; Yiemchaiyaphum, S.; Panich, S. Wrinkling Prediction of Rectangular Cup Deep Drawing Process for Aluminum Alloy Sheets by Using the Modified Yoshida Buckling Test. *Proc. Key Eng. Mater.* **2020**, *856*, 143–151. [CrossRef]
18. Du, B.; Xie, J.; Li, H.; Zhao, C.; Zhang, X.; Yuan, X. Determining Factors Affecting Sheet Metal Plastic Wrinkling in Response to Nonuniform Tension Using Wrinkling Limit Diagrams. *Thin-Walled Struct.* **2020**, *147*, 106535. [CrossRef]
19. Han, F.; Radonjic, R. New Approach for Wrinkle Prediction in Deep Drawing Process. *Key Eng. Mater.* **2015**, *639*, 459–466. [CrossRef]
20. Zein, H.; El Sherbiny, M.; Abd-Rabou, M. Thinning and Spring Back Prediction of Sheet Metal in the Deep Drawing Process. *Mater. Des.* **2014**, *53*, 797–808. [CrossRef]
21. El Sherbiny, M.; Zein, H.; Abd-Rabou, M. Thinning and Residual Stresses of Sheet Metal in the Deep Drawing Process. *Mater. Des.* **2014**, *55*, 869–879. [CrossRef]
22. Palmieri, M.E.; Nono Dachille, A.; Tricarico, L. Identification of the Optimal Blank Holder Force through In-Line Measurement of Blank Draw-In in a Deep Drawing Process. *J. Manuf. Mater. Process.* **2023**, *7*, 190. [CrossRef]
23. Kalujniy, O.V.; Kalujniy, V.L.; Aliiev, I.S.; Markov, O.E.; Levchenko, V.M. Investigation of Variants of Deep Drawing of Steel Hollow Parts. *J. Braz. Soc. Mech. Sci. Eng.* **2025**, *47*, 19. [CrossRef]
24. Kitayama, S.; Yamada, S. Simultaneous Optimization of Blank Shape and Variable Blank Holder Force of Front Side Member Manufacturing by Deep Drawing. *Int. J. Adv. Manuf. Technol.* **2017**, *91*, 1381–1390. [CrossRef]
25. Brun, M.; Ghiotti, A.; Simonetto, E.; Bruschi, S.; Filippi, S. Variable Blank Holder Pressure by Magneto-Rheological Actuators in Deep Drawing. *Proc. Procedia CIRP* **2023**, *119*, 932–937. [CrossRef]
26. Dong, F.; Huang, S.; Yi, Y.; He, H.; Huang, K.; Wang, C.; Gao, S.; Jia, Y.; Yu, W. Enhanced Deep Drawing Formability and Deformation Mechanism of Aluminum Alloy at Cryogenic Temperature. *J. Alloys Compd.* **2023**, *968*, 171992. [CrossRef]
27. Jang, D.H.; Kim, W.J. Warm Temperature Deformation Behavior and Processing Maps of 5182 and 7075 Aluminum Alloy Sheets with Fine Grains. *Met. Mater. Int.* **2018**, *24*, 455–463. [CrossRef]
28. Budai, D.; Tisza, M.; Kovács, P.Z. Investigation of EN AW 5754 Aluminum Alloy's Formability at Elevated Temperatures. *Proc. Mater. Sci. Forum* **2017**, *885*, 98–103. [CrossRef]
29. Do, T.T.; Minh, P.S.; Le, N. Effect of Tool Geometry Parameters on the Formability of a Camera Cover in the Deep Drawing Process. *Materials* **2021**, *14*, 3993. [CrossRef]
30. Li, Y.Q.; Cui, Z.S.; Ruan, X.Y.; Zhang, D.J. CAE-Based Six Sigma Robust Optimization for Deep- Drawing Process of Sheet Metal. *Int. J. Adv. Manuf. Technol.* **2006**, *30*, 631–637. [CrossRef]
31. Jweeg, M.J.; Mohammed, A.I.; Jabbar, M.S. Investigation of Thickness Distribution Variation in Deep Drawing of Conical Steel Products. *Eng. Technol. J.* **2021**, *39*, 586–598. [CrossRef]
32. Dilmec, M.; Halkaci, H.S.; Ozturk, F.; Livatyali, H.; Yigit, O. Effects of Sheet Thickness and Anisotropy on Forming Limit Curves of AA2024-T4. *Int. J. Adv. Manuf. Technol.* **2013**, *67*, 2689–2700. [CrossRef]
33. Mostafa, M.; Abdelbarr, M.; Hassab-Allah, I.M.; Bayummi, A.; Shewakh, W.M. Optimum Process Parameters for Increasing the Drawability of Square Cup Though Conical Die. *J. Adv. Eng. Trends* **2023**, *42*, 141–153.
34. Hassan, M.; Hezam, L.; El-Sebaie, M.; Purbolaksono, J. Deep Drawing Characteristics of Square Cups through Conical Dies. *Proc. Procedia Eng.* **2014**, *81*, 873–880. [CrossRef]
35. Brathikan, V.M.; Sangeetha, N.; Sangeethkumar, B.; Scidarth, K. Influence of Various Blank Diameter in Deep Drawing. *Mater. Today Proc.* **2022**, *68*, 1995–1999. [CrossRef]
36. Lazarescu, L.; Nicodim, I.; Banabic, D. Evaluation of Drawing Force and Thickness Distribution in the Deep-Drawing Process with Variable Blank-Holding. *Key Eng. Mater.* **2015**, *639*, 33–40. [CrossRef]
37. Leelaseat, J.; Larpprasoetkun, P.; Sunanta, A.; Nakwattanaset, A.; Suranuntchai, S. Investigation on the Effect of Blank Holder Force and Initial Blank Size on the Thinning Problem of the Fuel Tank Part Made from Aluminum Alloy Sheet 5754-O under Deep Drawing Process. *Key Eng. Mater.* **2024**, *973*, 101–107. [CrossRef]
38. Sun, G.; Li, G.; Gong, Z.; Cui, X.; Yang, X.; Li, Q. Multiobjective Robust Optimization Method for Drawbead Design in Sheet Metal Forming. *Mater. Des.* **2010**, *31*, 1917–1929. [CrossRef]
39. Alves, J.L.; Bouvier, S.; Oliveira, M.C.; Menezes, L.F. Drawbeads: To Be or Not to Be. *AIP Conf. Proc.* **2005**, *778*, 655–660.
40. Bae, G.H.; Song, J.H.; Huh, H.; Kim, S.H.; Park, S.H. Simulation-Based Prediction Model of the Draw-Bead Restraining Force and Its Application to Sheet Metal Forming Process. *J. Mater. Process Technol.* **2007**, *187*, 123–127. [CrossRef]

41. Ke, J.; Liu, Y.; Zhu, H.; Zhang, Z. Formability of Sheet Metal Flowing through Drawbead—An Experimental Investigation. *J. Mater. Process Technol.* **2018**, *254*, 283–293. [CrossRef]
42. Panich, S.; Uthaisangsuk, V. Wrinkling Limit Curves with Consideration of Anisotropic Behaviour for the Deep Drawing of Aluminium Sheet Alloys. *Proc. Inst. Mech. Eng. Part L J. Mater. Des. Appl.* **2023**, *237*, 592–615. [CrossRef]
43. Senior, B.W. Flange Wrinkling in Deep-Drawing Operations. *J. Mech. Phys. Solids* **1956**, *4*, 235–246. [CrossRef]
44. Hilton, P.; Pedersen, J. Looking into Pascal's Triangle: Combinatorics, Arithmetic, and Geometry. *Math. Mag.* **1987**, *60*, 305–316. [CrossRef]
45. *ASTM E8/E8M-16a*; Standard Test Methods for Tension Testing of Metallic Materials. ASTM International: West Conshohocken, PA, USA, 2016.
46. Swift, H. Plastic Instability under Plane Stress. *J. Mech. Phys. Solids* **1952**, *1*, 1–18. [CrossRef]
47. ESI Group. *PAM-STAMP 2022.0—User Guide*; ESI Group: Bagneux, France, 2022.
48. Hill, R. A Theory of the Yielding and Plastic Flow of Anisotropic Metals. *Proc. R. Soc. Lond. A Math. Phys. Sci.* **1948**, *193*, 281–297.
49. Barlat, F.; Lian, K. Plastic Behavior and Stretchability of Sheet Metals. Part I: A Yield Function for Orthotropic Sheets Under Plane Stress Conditions. *Int. J. Plast.* **1989**, *5*, 51–66.
50. Xu, S.G.; Bohn, M.L.; Weinmann, K.J. Drawbeads in Sheet Metal Stamping—A Review. In *SAE Technical Papers*; SAE International: Warrendale, PA, USA, 23 February 1997.
51. Karnchanaseangthong, T.; Inpunyo, C.; Torsakul, S. A Study of the Effect of Drawbead Shapes in Non-Symmetry Deep Drawing Process by Using Finite Element-Simulation. *Thai Ind. Eng. Netw. J.* **2016**, *2*, 15–22.
52. Phanitwong, W.; Thipprakmas, S. Analysis of Draw Bead Geometry on Wall Thinning and Concave/Convex Feature in Rectangular Deep Drawn Parts. *Adv. Mat. Res.* **2011**, *189*, 2704–2707. [CrossRef]
53. Larpprasoetkun, P.; Leelaseat, J.; Nakwattanaset, A.; Suranuntchai, S. Development of Forming Limit Diagrams for Motorcycle Fuel Tank Made from AA5754-O under Deep Drawing. *J. Met. Mater. Miner.* **2024**, *34*, 2013. [CrossRef]
54. Cao, J.; Boyce, M.C. Wrinkling Behavior of Rectangular Plates under Lateral Constraint. *Int. J. Solids Struct.* **1997**, *34*, 153–176. [CrossRef]
55. Triantafyllidis, N. Puckering Instability Phenomena in the Hemispherical Cup Test. *J. Mech. Phys. Solids* **1985**, *33*, 117–139. [CrossRef]
56. Wang, X.; Cao, J. On the Prediction of Side-Wall Wrinkling in Sheet Metal Forming Processes. *Int. J. Mech. Sci.* **2000**, *42*, 2369–2394. [CrossRef]
57. Bassoli, E.; Sola, A.; Denti, L.; Gatto, A. Experimental Approach to Measure the Restraining Force in Deep Drawing by Means of a Versatile Draw Bead Simulator. *Mater. Manuf. Process.* **2019**, *34*, 1286–1295. [CrossRef]

Disclaimer/Publisher's Note: The statements, opinions and data contained in all publications are solely those of the individual author(s) and contributor(s) and not of MDPI and/or the editor(s). MDPI and/or the editor(s) disclaim responsibility for any injury to people or property resulting from any ideas, methods, instructions or products referred to in the content.